CFSRC COLLOQUIUM

Proceedings of the Cold-Formed Steel Research Consortium Colloquium
17-19 October 2022 (cfsrc.org)

Numerical Implementation of GMNIA for Steel Frame with Nonsymmetric Sections

Liang Chen[1], Weihang Ouyang[2], Si-Wei Liu[3]*, and Ronald D. Ziemian[4]

Abstract

Steel members using nonsymmetric sections are often used for their structural efficiency in contemporary construction. However, traditional inelastic analysis methods are mostly derived from regular hot-rolled steel sections with symmetrical shapes; the adoption of those methods may lead to significant differences when analyzing members with nonsymmetric sections. In view of such a need, this research proposed an innovative method for the Geometrically and Materially Nonlinear Analysis with Imperfections (GMNIA) of steel frame with symmetric and nonsymmetric sections. An improved line-element formulation derived based on its principal axis is adopted. The tangent stiffness matrix of the element is formulated based on the nonsymmetric section assumption, explicitly modeling the noncoincidence of the shear center and centroid for considering the Wagner effects. The proposed line-element can capture complex buckling behaviors of the members with nonsymmetric sections. Then, the Concentrated plasticity (CP) model is integrated into the element tangent stiffness matrix to consider the material nonlinearity, where the full-yield criterion using the yield surface is adopted. As part of this, a rigorous cross-section analysis method has been developed to generate the yield surfaces of arbitrary steel sections regardless of shapes. Such yield surfaces will be used to evaluate the full-yield condition, and the gradients to the yield surfaces will be calculated and used to control the plastic flow. The development of this GMINA for steel frame with nonsymmetric sections is presented in detail, as well as the derivation of the mathematical formulations. At last, two groups of verification examples are provided to validate the accuracy of the yield surface generation method and the proposed GMINA.

1. Introduction

Steel members with nonsymmetric cross-sections (Fig. 1) are often used in civil engineering structures because they can significantly improve material efficiency. The disadvantage in fabricating nonsymmetric cross-sections is no longer as significant because most steel members can be formed and/or robotically welded, thereby enabling arbitrary shapes to be made easily and economically. In general, modern structural design relies on the robustness of the analysis method to assess the ultimate strength behavior of structural systems. Design methods based on advanced analysis, however, are mainly provided for regular hot-rolled or welded sections with symmetrical shapes. Their adoption for designing with nonsymmetric cross-sections is sometimes inapplicable. As a result, potential gains in efficiency are limited.

The successful structural design for steel structures requires a realistic assessment of the ultimate strength capacity of a structure under extreme loading conditions, such as super-typhoon and seismic events, to ensure structural safety. As such, geometrically and materially nonlinear analysis with imperfections (GMNIA), which include geometric (second-order) and material (inelastic) nonlinear effects, is crucial and has been extensively studied over the past 65 years [1-8]. The research presented herein mostly adopts the concentrated plasticity (plastic hinge) analysis method for inelastic simulation, aiming for practical application via efficient computational procedures. The modified tangent modulus (MTM) approach, proposed by Ziemian and McGuire [9], is an implementation of plastic hinge analysis methods that have been used widely for nearly two decades, thereby establishing its robustness and effectiveness. This method has been used in designing systems of hot-rolled steel members with symmetric section shapes and is now expanded in the present study to promote its application for systems of nonsymmetric steel section members.

When analyzing steel members with nonsymmetric sections, another dominant consideration is using line-elements for frame analysis that can simulate the offset

[1] Ph.D Candidate, The Hong Kong Polytechnic University, Hong Kong, China, E-mail: liang17.chen@connect.polyu.hk
[2] Ph.D Student, The Hong Kong Polytechnic University, Hong Kong, China, E-mail: weihang.ouyang@connect.polyu.hk
[3] Assistant Professor, The Hong Kong Polytechnic University, Hong Kong, China, (corresponding author) E-mail: si-wei.liu@polyu.edu.hk
[4] Professor, Department of Civil and Environmental Engineering, Bucknell University, USA, E-mail: ziemian@bucknell.edu

between the shear center and the centroid of the cross-section. Several line-elements have been derived for including such effects. For example, beam elements using co-rotational (CR) formulation for nonsymmetric sections are proposed by Hsiao and Lin [10] and Battini and Pacoste [11]. Several displacement-based line-elements have also more recently been developed that further include the Wagner effects, including work by Liu et al. [12] and Rinchen et al. [13]. It should be noted that such element formulation must be established by referring to the section principal axis rather than the geometric axis, thereby representing the proper element deflection directions for the given external loading [14]. The line-element formulation, developed by Liu et al. [14], is employed in this paper. Some recent research has used this element for studying the elastic and buckling behaviors of steel structures with nonsymmetric sections [15, 16], and the related research about the steel structures with nonsymmetric sections has been continuously studied until now [17, 18].

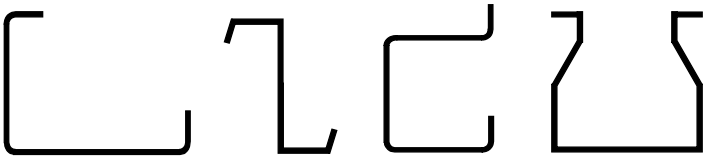

Fig. 1 Typical examples of nonsymmetric steel sections

In this research, the concentrated plasticity (CP) model is integrated into the element tangent stiffness matrix, and the MTM approach is adopted to represent partial material yielding, which may be accentuated by the residual stresses. A yield surface, describing the full yield capacity of a section resisting axial force and major-axis bending and/or minor-axis bending, is required. For hot-rolled steel sections with symmetric shapes, a governing equation proposed by McGuire et al. [19] is commonly used (Fig. 2 a) but has long been recognized as unsuitable for nonsymmetric sections (Fig. 2 b). With this in mind, a cross-section analysis method for calculating the yield surface of arbitrary sections (both symmetric and nonsymmetric) is proposed and uses the fibre section model as developed based on the Quasi-Newton divergence-free algorithm proposed by Liu et al. [20]. A matrix describing the gradients at all points on the yield surface will be used to control the plastic flow.

Table 1. provides a summary of the features of different GMNIA methods for designing steel systems comprised of nonsymmetric sections, with such methods including the shell finite-element method (SFEM) [21-23], the finite-strip method (FSM) [24-26], the original MTM method [9], and the present CP-MTM approach.

This paper first presents the assumptions of this research and a brief formulation of the line-element employed for modeling nonsymmetric section. After providing the approach to implement the CP-MTM approach, a divergence-free cross-section analysis algorithm using the fibre section model is proposed to evaluate the full-yield criterion. Finally, the inelastic response and validation are elaborated, which is followed by a summary and conclusion section.

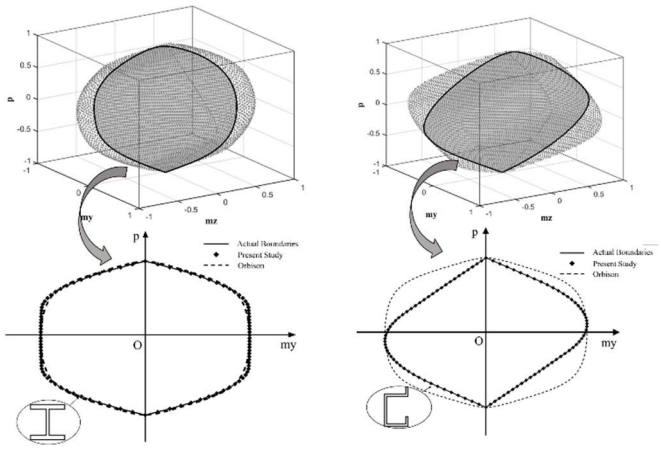

(a) Symmetric section (b) Nonsymmetric section

Fig. 2 Illustrations of the yield surfaces

Table 1. The features of different nonlinear analysis methods for investigating steel members with nonsymmetric sections

		Numerical solutions			
				MTM method	
		SFEM	FSM	Original	Present study
Geometrical Nonlinearity	Large deflection	✓	✓	✓	✓
	Warping	✓	×	×	✓
	Wagner effects	✓	×	×	✓
Elastic-plasticity	Inelastic behaviors	✓	✓	✓	✓
	Failure criterion	✓	×	✓	✓
	Plastic flow control	✓	✓	✓	✓
Initial imperfections	Residual stress	✓	×	✓	✓
	Geometrical Imperfections	✓	✓	✓	✓
Numerical implementation	Computational efficiency	*	**	***	***
	Programming difficulty	***	**	*	**
Practical application	Member design	✓	✓	✓	✓
	System design	×	×	✓	✓

Note: A cross (×) indicates that it is not applicable whilst a check (✓) indicates that it is applicable. The symbol (*) represents the efficiency and difficulty level in 3-degrees scale (e.g. "*" is low and "***" is high).

2. Assumptions

The following assumptions are made: (1) material remains elastic in the element; however, the deformation due to material yielding is concentrated at potential plastic hinges at the element ends; (2) Plane sections remain plane after deformation; (3) the applied loads are conservative; (4) the Euler-Bernoulli beam assumption is made without varied the shear strain over the cross-section, but warping deformation is considered; (5) strain within the element is small, whereas

the element deformation can be moderately large via the Updated-Lagrangian formulation used; (6) local buckling and distortional buckling are not considered; and (7) the material's constitutive model for steel is taken as linearly elastic-perfectly plastic.

3. Line-Element Formulation

An improved line-element formulation was recently developed by Liu et al. [14] and employed in the present study. When analyzing steel members with nonsymmetric sections, the dominant features using line-elements for frame analysis include: (1) the element formulations should be derived based on the principal section axis; and (2) the Wagner effects and the noncoincidence of the shear center and centroid of a nonsymmetric section should be considered. This element can capture the nonlinear and buckling behaviors of members with nonsymmetric sections, evidenced by the extensive validations [12, 14, 27-29]. This research extends its application for the GMNIA by integrating the CP model into the element tangent stiffness matrix.

3.1 Total potential energy

The detailed derivation can be found in the reference [14], which will be concisely elaborated as follows. There are 14 degree-of-freedoms (DOFs) within the element (Fig. 3), as given below.

$$[u] = [u_1 \quad v_1 \quad w_1 \quad \theta_{x1} \quad \theta_{v1} \quad \theta_{w1} \quad \theta_{b1} \quad u_2 \quad v_2 \quad w_2 \quad \theta_{x2} \quad \theta_{v2} \quad \theta_{w2} \quad \theta_{b2}] \tag{1}$$

where, u, v, and w are the displacements along the element local axes; θx, θv, and θw are the rotations about the element local axes; and θb is the warping deformation. The subscript 1 and 2 stand for the element start and end nodes, respectively.

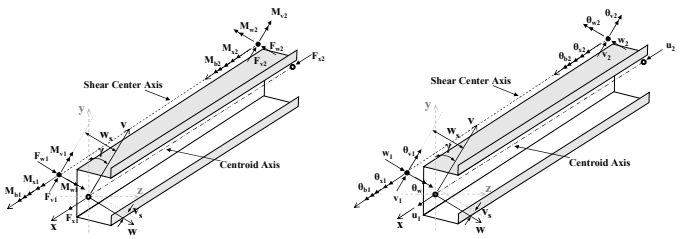

(a) Local Element Forces (b) Local DOFs

Fig. 3 The DOFs and nodal forces within the line-element.

The corresponding nodal forces are,

$$[f] = [F_{x1} \quad F_{v1} \quad F_{w1} \quad M_{x1} \quad M_{v1} \quad M_{w1} \quad M_{b1} \quad F_{x2} \quad F_{v2} \quad F_{w2} \quad M_{x2} \quad M_{v2} \quad M_{w2} \quad M_{b2}] \tag{2}$$

There are two coordinate systems for the members with nonsymmetric sections. One is the y-o-z coordinate system as the element local axis, and the other is the principal coordinate system (v-o-w). γ is the inclined angle between those two coordinate systems.

The strain in the element can be defined via the shape functions, given by McGuire et al. [19]:

$$\begin{aligned} \psi_u = N_1 u_1 + N_2 u_2;\ \psi_v = N_3 v_2 + N_4 v_1 + N_5 \theta_{1w} - N_6 \theta_{2w} \\ \psi_w = N_3 w_2 + N_4 w_1 - N_5 \theta_{1v} + N_6 \theta_{2v}; \\ \psi_\theta = N_5 \theta_{b1} + N_6 \theta_{b2} + N_4 \theta_{x1} + N_3 \theta_{x2} \end{aligned} \tag{3}$$

where, *ψu, ψv,* and *ψw* describe the displacements along the x-, v-, and w- axes, respectively; ψθ describes the twisting about the x- axis. N1 to N6 are the coefficients for the shape-function given as,

$$\begin{aligned} N_1 = 1 - \frac{x}{L},\ N_2 = \frac{x}{L},\ N_3 = \frac{3x^2}{L^2} - \frac{2x^3}{L^3} \\ N_4 = 1 - \frac{3x^2}{L^2} + \frac{2x^3}{L^3},\ N_5 = x - \frac{2x^2}{L} + \frac{x^3}{L^2},\ N_6 = \frac{x^2}{L} - \frac{x^3}{L^2} \end{aligned} \tag{4}$$

where, L stands for the length of the element, and x is the axial coordinate along the element.

The element tangent stiffness matrix can be generated by the second variation of the total potential energy function Π,

$$\Pi = U - V \tag{5}$$

in which U is the element strain energy and V is the work done by the external forces. The strain energy U can be computed by integrate the Green-Lagrange strains generated from the shape-functions and the corresponding stress expressed by referring to the nodal forces.

3.2 Tangent stiffness matrix

According to the minimum potential energy principle, the element stiffness matrices can be generated from the second variation of the total potential energy Π,

$$\delta^2 \prod = \frac{\delta^2 \prod}{\delta d_i \delta d_j} \delta d_i \delta d_j = [k_e][\Delta u] - [\Delta f] = 0 \tag{6}$$

in which, [Δu] and [Δf] are the displacement increment and force increment, and [ke] is the element stiffness matrix, which can be generated by,

$$[k_e] = [T]([k_L][T_L] + [k_G] + [k_U])[T]^T \tag{7}$$

where $[k_L]$ has been well established and documented by McGuire et al. [19]; $[k_G]$ and $[k_U]$ are geometric stiffness matrices for symmetric and nonsymmetric sections, respectively; $[T]$ and $[T_L]$ are the transformation matrices given by Liu et al. [14].

4. Modified Tangent Modulus (MTM) Method

This research extends the application of the line-element formulation given above by integrating the CP model into the

element tangent stiffness matrix. The zero-length plastic hinges at the element ends will be used to account for the material nonlinearity. In addition, the MTM approach [9], which is a straightforward extension of the CP model, is adopted to represent partial material yielding of the cross-section.

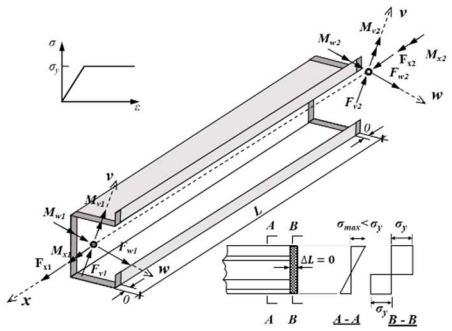

Fig. 4. Concentrated plasticity (CP) model

4.1 Concentrated plasticity (CP) model

The CP model is adopted to consider the material nonlinearity in this research. The total plastic flexural deformation is represented by a zero-length hinge located at one or both ends of the element. The illustration of a CP model with elastic-perfectly-plastic material constitutive is shown in Fig. 4. Using the CP model can avoid complicated and tedious stress resultant formulation, which is more effective and acceptable when performing the inelastic analysis for massive practical structures.

4.2 Implementation

The MTM approach is a straightforward extension of the CP method, which has been used widely for nearly two decades. This research adopts the MTM method to represent partial material yielding, which may be accentuated by the residual stresses. In the MTM method, a reduction factor τ is given for reducing the element tangent stiffness, which is expressed as,

$$E_{tm} = \tau E \; with \; \tau = min\begin{Bmatrix} 1.0 \\ (1+2p)(1-p-\alpha_v m_v - \alpha_w m_w^2) \end{Bmatrix} \quad (8)$$

in which, $p = |P/P_x|$, $m_v = \left|M_v/M_{pv}\right|$, and $m_w = \left|M_w/M_{pw}\right|$. $\alpha_v$and α_w are the empirical factors and the values, 0.65 and 1.0, given by Ziemian and McGuire [9], are adopted.

The factor τ is related to the *p*, m_v, and m_w values. The corresponding relationships between τ and those values in some general cases are shown in **Fig. 5**.

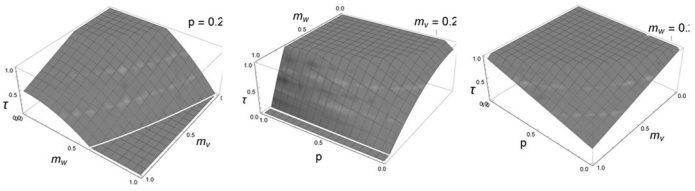

(a) When p = 0.2 (b) When m_v = 0.2 (b) When m_w = 0.2

Fig. 5. Plots of the τ factor.

The stiffness along the element can be generated by,

$$E(x) = [(1 - x/L)a + b\,x/L]E \quad (9)$$

where, a and b are the reduction factors given by,

$$a = E_{tm,1}/E;\; b = E_{tm,2}/E \quad (10)$$

in which, $E_{tm,1}$ and $E_{tm,2}$ are the reduced material Young's modulus at the element ends, and the element tangent stiffness matrix given in Equation (7) can be rewritten as.

$$[k_e] = [T]\left([\rho_{et}] \odot [k_L][T_L] + [k_g] + [k_u]\right)[T]^T \quad (11)$$

where $\odot$ represents the Hadamard product, $[\rho_{et}]$ is the reduction matrix given in [30].

5. Full-yield Criterion Using a Yield Surface

The plastic hinge will eventually form at the ends of the member with the increment of applied forces. This research adopts the full-yield criterion using a yield surface that describes the full yield capacity of a section resisting axial force and major-axis moment and minor-axis moment (**Fig. 6**).

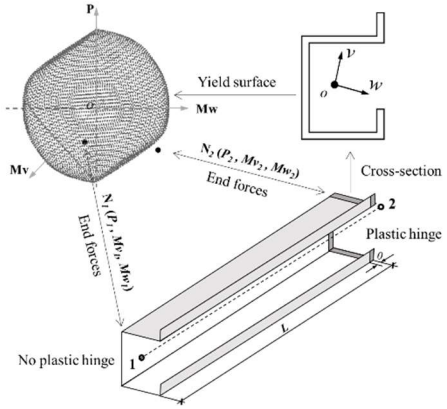

Fig. 6. The full-yield criterion using a yield surface

5.1 Full-yield criterion

The basic concepts of the full-yield criterion using yield surface are: (1) sections with force points lie within the yield surface are elastic; (2) sections for which the force points on the yield surface are fully plastic; and (3) points outside the yield surface are not admissible because the material's constitutive model for steel is assumed to be linearly elastic-perfectly plastic. This research proposed a numerical method to estimate whether a force point, like N [*P, M_v, M_w*],

is located inside the yield surface or not. As shown in **Fig. 7**, there is a spatial yield surface with the origin point O. When a section internal forces are *P*, *Mv*, and *Mw*, which can be denoted as point N, there will be an intersection point, N_1 [P_1, M_{v1}, M_{w1}], between the extended line of OP and the yield surface, as shown in **Fig. 7**. The corresponding loading ratio L_r will be calculated by,

$$L_r = d/d_1 \tag{12}$$

where *d* and d_1 are the norm of the vector [*P*, M_v, M_w] and [P_1, M_{v1}, M_{w1}], respectively.

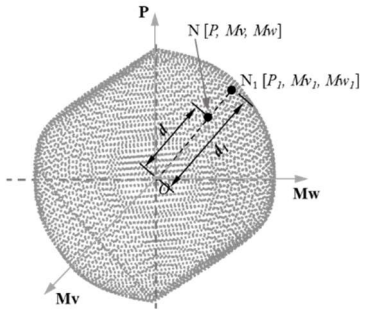

Fig. 7. A spatial yield surface

When $L_r < 1.0$ indicates that the point N is located inside the yield surface and the related section is elastic. When $L_r = 1.0$, the point N is on the yield surface, and the corresponding section will be regarded as fully plastic. And if $L_r > 1.0$, the point N is outside the yield surface, which is not admissible, a correction of the resisting forces will be conducted.

A spatial yield surface (**Fig. 7**), describing the ultimate strength capacity of a section for the axial force and major-axis moment and minor-axis moment, is required and essential for the yield criterion. For the hot-rolled sections with doubly symmetric section shapes, the yield surface can be easily calculated with the equations given by ANSI/AISC-360-16 [31] or McGuire et al. [19], where the yield surfaces are also symmetric in shape. Nevertheless, the yield surfaces are nonsymmetric for nonsymmetric sections, which cannot be generated by the conventional equations. Apart from deriving the curve-fitted equations, a rigorous analysis method to calculate the yield surfaces for any section shapes is developed based on the work introduced by Liu et al. [20].

5.2 Cross-section modelling

A cross-section modelling approach has been proposed for the calculation of the yield surfaces. The cross-section will be modelled by nodes and segments, as shown in **Fig. 7**, where the segments are the centerline of the section plate, and the nodes are the starting, ending, and intersection of the segments. Each segment is defined by two nodes and a thickness, and the initial coordinates of the nodes are given based on a global Z-O-Y coordinate system.

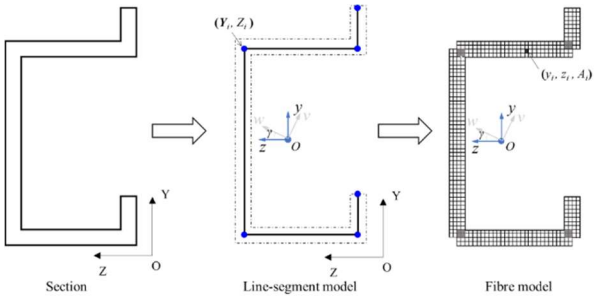

Fig. 8 Cross-section modelling

The coordinate of the cross-section centroid can be computed by,

$$Z_o = \frac{\sum_{i=1}^{n_S} L_i t_i (Z_{Li}+Z_{Ri})/2}{A} \text{ and } Y_o = \frac{\sum_{i=1}^{n_S} L_i t_i (Y_{Li}+Y_{Ri})/2}{A} \tag{13}$$

where n_S is the number of the segments in the cross-section; the subscripts $_i$ denote the i^{th} segment; the subscripts $_L$ and $_R$ indicates the start and end nodes of the segment; L_i stands for the segment length. A new local coordinate system with the centroid as the origin (i.e., z-o-y system) will established and the coordinates (z_i, y_i) of the i^{th} node can be calculated by,

$$z_i = Z_i - Z_o \text{ and } y_i = Y_i - Y_o \tag{14}$$

As shown in **Fig. 7**, the section principal coordinate system (i.e., w-o-v system) will also be established, where γ is the angle between the y-o-z system and v-o-w system given by,

$$\gamma = 0.5 tan^{-1}\left[2I_{yz}/\left(I_y - I_z\right)\right] \tag{15}$$

in which, I_z, I_y, and I_{yz} are the section properties calculated by,

$$I_z = \int_A y^2 dA = \sum_{i=1}^{n_S} \left(\frac{y_{Li}+y_{Ri}}{2}\right)^2 L_i t_i + \frac{1}{12}(y_{Li}-y_{Ri})^2 L_i t_i \tag{16}$$

$$I_y = \int_A z^2 dA = \sum_{i=1}^{n_S} \left(\frac{z_{Li}+z_{Ri}}{2}\right)^2 L_i t_i + \frac{1}{12}(z_{Li}-z_{Ri})^2 L_i t_i \tag{17}$$

$$I_{yz} = \int_A yz dA = \sum_{i=1}^{n_S} \left(\frac{z_{Li}+z_{Ri}}{2}\right)\left(\frac{y_{Li}+y_{Ri}}{2}\right) L_i t_i + \frac{1}{12}(z_{Li}-z_{Ri})(y_{Li}-y_{Ri}) L_i t_i \tag{18}$$

Then, as shown in **Fig. 7**, the segments of the section will be further meshed into small fibres. Each fibre is described by the coordinates of its centroid (y_i, z_i), referring to z-o-y system, and the fibre area (A_i). During the analysis procedure, the principal v-o-w axis system will be used to calculate stress resultants. The fibre centroid coordinates in v-o-w system (w_i,v_i) can be calculated by,

$$[v_i \quad w_i]^T = \begin{bmatrix} cos\,\gamma & -sin\,\gamma \\ sin\,\gamma & cos\,\gamma \end{bmatrix} [y_i \quad z_i]^T \tag{19}$$

5.3 Yield surface generation

As shown in **Fig. 9**, the strain is linearly distributed in the cross-section according to the Euler-Bernoulli hypothesis. The stress at each fibre can be determined based on the strain level. By referring to the v-w axis system, the overall section capacity can be calculated by the equations as follows to get one data point of the yield surface.

$$P = \sum_{i=1}^{nf} \sigma_i(\varepsilon_i)A_i,\ M_v = -\sum_{i=1}^{nf} \sigma_i(\varepsilon_i)A_i w_i, \text{ and } M_w = \sum_{i=1}^{nf} \sigma_i(\varepsilon_i)A_i v_i \quad (20)$$

where P, M_v and M_w are the section ultimate axial and bending capacities, respectively, n_f is the total number of fibers, v_i and w_i are the coordinates in principal axis, and σ_i represents the i^{th} fibre's stress generated from constitutive models, and ε_i is i^{th} fibre's strain, which can be calculated by,

$$\varepsilon_i = \varepsilon_u d_i / d_n \quad (21)$$

in which, ε_u is the strain of the topmost fiber, which equals to the material ultimate strain, d_n is the location of the neutral axis (**Fig. 9**), and d_i is the location of the i^{th} fibre, whose value will be negative if the i^{th} fibre is on the other side of the neutral axis.

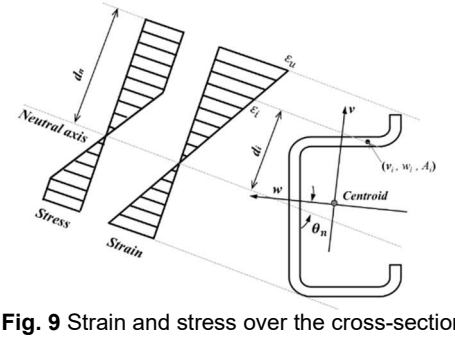

Fig. 9 Strain and stress over the cross-section

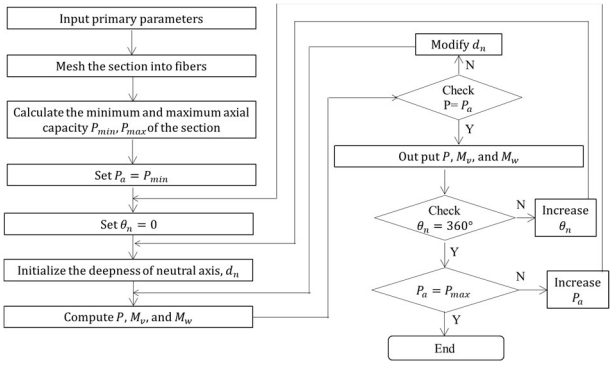

Fig. 10. A flowchart to generate the complete yield surface

The complete yield surface of any sections can be generated by changing the axial load P_a from the minimum axial strength (tension capacity) to the maximum axial strength (compression capacity) and rotating the inclined angle between the neutral axis and the principal axis θ_n (**Fig. 9**) from 0 to 2π at each axial load P_a. At a certain angle θ_n, the strain of the topmost fiber will be assumed to be the ultimate strain ε_u, then the location of the neutral axis d_n will be calculated using the Quasi-Newton algorithm.

$$d_n^{k+1} = d_L^k + \frac{d_U^k - d_L^k}{P_U^k - P_L^k}\left(P_a - P_L^k\right) \quad (22)$$

where d_n^{k+1} is the location of the current neutral axis; d_U^k is the location of neutral axis with the axial force P_U^k larger than P_a; and d_L^k is the location of neutral axis with the axial force P_L^k smaller than P_a. Detailed iteration procedure can be found in reference paper [32]. Once the location of the updated neutral axis is determined, one data point of the yield surface can be generated with Equation (20). The analysis flowchart for the generation of the complete yield surface is elaborated in **Fig. 10**, which has been implemented within the MSA_Sect module in Mastan2 v6 [33]. The calculation procedure will give a series of data points, which will form a complete yield surface, as shown in **Fig. 7**.

6. Post Yielding Behavior

According to the assumption, the plastic deformation will be only concentrated on the end of an element in the CP model. Once the internal member forces point has reached the yield surface, the member may either remain plastic with the force point moving along the yield surface or unload elastically with the force point moving into the yield surface. In this research, the gradient matrix describing the gradients to the yield surface will be calculated to control the plastic flow.

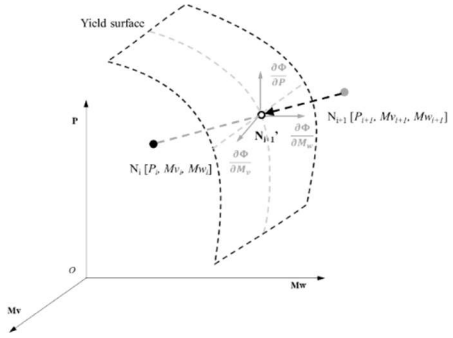

Fig. 11. Correction of force point outside the yield surface

6.1 Correction of force point outside the yield surface

When the loading ratio L_r from Equation (12) is larger than 1.0, it indicates that the force point lies outside the failure surface, which is not admissible. As shown in **Fig. 11**, at the i^{th} load step, the element end forces are assumed as N_i [P_i, M_{vi}, M_{wi}]. This force point is inside the yield surface, which shows that there is no plastic deformation. While in the next load increment, the force point is increased to N_{i+1} [P_{i+1}, M_{vi+1}, M_{wi+1}], which is outside the yield surface. There are millions of paths to bring this force point back onto the yield surface. In this paper, the path connecting N_i and N_{i+1} is chosen and the new equilibrium force point will be N_{i+1}', as

shown in **Fig. 11**. The coordinate of the N_{i+1}' will be taken as the new resisting forces.

6.2 The plastic reduction matrix

The incremental displacement at a plastic hinge can be divided into two parts: the elastic and a plastic displacement:

$$[d\Delta] = [d\Delta_e] + [d\Delta_p] \quad (23)$$

As shown in **Fig. 12**, since the increment of plastic deformation must be normal to the yield surface, the plastic deformation $[d\Delta_p]$ can be acquired by the gradients to the yield surface:

$$[d\Delta_{p1}] = \lambda_1[G_1] \quad (24)$$

$$[G_1] = \left[\frac{\partial \Phi}{\partial P_1} \quad \frac{\partial \Phi}{\partial M_{v1}} \quad \frac{\partial \Phi}{\partial M_{w1}}\right]^T \quad (25)$$

where Φ represents the function of the entire yield surface obtained by the proposed method and $[G_1]$ is the gradient to it; and λ_1 is the magnitude of the plastic deformation.

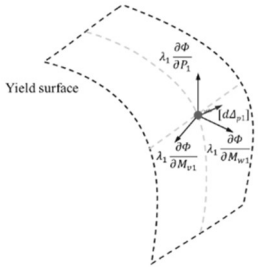

Fig. 12. Plastic deformation

Since both ends of the element have the possibility of plastification, the element's plastic deformation can be expressed as:

$$[d\Delta_p] = \begin{bmatrix} d\Delta_{p1} \\ d\Delta_{p2} \end{bmatrix} = \begin{bmatrix} [G_1] & 0 \\ 0 & [G_2] \end{bmatrix} \begin{bmatrix} \lambda_1 \\ \lambda_2 \end{bmatrix} = [G][\lambda] \quad (26)$$

in which, $[G]$ is a matrix and a vital component of the derivation of the plastic reduction matrix. The matrix $[G]$ contains nonzero elements only when the element ends in the plasticized situation. The primary purpose of this matrix is to reduce axial and rotational resistance.

The linearly elastic-perfectly plastic constitutive model is adopted for steel. Therefore, all the force points located on the yield surface will remain plastic, with the force points moving along the yield surface. Consequently, any incremental of the force vector at those points must follow the elastic relationship:

$$[dF] = [k_e][d\Delta_e] \quad (27)$$

in which $[d\Delta_e]$ is the incremental elastic deformation.

When the plastic deformation has been accessed by Equation (25), the plastic deformation and the incremental force vectors will be orthometric and the following expression can be attained:

$$[d\Delta_p][dF] = [\lambda][G]^T[dF] = 0 \quad (28)$$

Since [λ] is arbitrary, the above expression can be simplified as,

$$[G]^T[dF] = 0 \quad (29)$$

Using Equations (12), (25), (26), and (28), and solving for $[\lambda]$, the solution can be got:

$$[\lambda] = \left[[G]^T[k_e][G]\right]^{-1}[G]^T[k_e][d\Delta] \quad (30)$$

Similarly, using Equations (12), (25), (26), and (29) and solving for $[dF]$ results in

$$[dF] = \left[[k_e] + [k_m]\right][d\Delta] \quad (31)$$

in which, $[k_m]$ is the element plastic reduction matrix, which can be generated by,

$$[k_m] = -[k_e][G]\left[[G]^T[k_e][G]\right]^{-1}[G]^T[k_e] \quad (32)$$

6.3 Gradients to the yield surface

For tracing the plastic deformations, the gradients to the yield surface need to be calculated. The yield surface generated by the proposed numerical method consists of a series of discrete data points, as shown in **Fig. 12.** This yield surface is too complicated to be described with curve-fitted equations. Therefore, a numerical method that is reasonable and practical for computing the gradients to the discrete point on the yield surface has been proposed.

The gradient on a data point of the yield surface will be calculated by,

$$\boldsymbol{\Phi}'(N) = \frac{[n_1] + [n_2] + [n_3] + [n_4]}{|[n_1] + [n_2] + [n_3] + [n_4]|} \quad (33)$$

in which, $[n_1]$, $[n_2]$, $[n_3]$, and $[n_4]$ are the normal vectors of the areas around the data point (**Fig. 12**). The gradients to each data point on the yield surface will be calculated with the above equation and used to control the plastic flow.

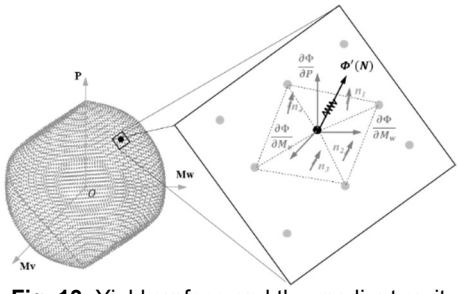

Fig. 13. Yield surface and the gradient on it

7. Numerical Procedure

In present study, an incremental stiffness method based on the Updated-Lagrangian (UL) approach is employed to account for the influence of large deflections on the

distribution of internal forces. The UL method is efficient and robust, especially when the element formulation involves large deformations.

7.1 Global stiffness matrix and element resistant forces

In the proposed incremental stiffness method, the global stiffness matrix will be assembled by,

$$[K_E] = \sum_{m=1}^{NE} ([\Gamma]^T [[k_e] + [k_m]][\Gamma]) \quad (34)$$

where $[k_e]$ is the element tangent stiffness matrix generated by Equation (11), $[k_m]$ is the element plastic reduction matrix calculated by Equation (32), *NE* represents the total number of elements, and $[\Gamma]$ is the transformation matrix given by McGuire et al. [19].

With the element global stiffness matrix, the element incremental forces can be calculated by,

$$[\Delta R_e^i] = [K_E]^i \Delta u_e^i \quad (35)$$

where the superscript ^{i} denotes the *ith* incremental step, Δu_e^i is the element incremental displacement without rigid body movement [12]. And, then the element total forces can be updated by,

$$[R_e^{i+1}] = [R_e^i] + [\Delta R_e^i] \quad (36)$$

7.2 Analysis procedure

The flowchart of the numerical analysis procedure for the proposed GMNIA is given in [30]. Firstly, the basic information, including the geometries of the analytical model and cross-section dimension, material parameters, boundary conditions, and the like, are inputted into the program. Then, the section properties, yield surface, and gradients to the yield surface are calculated. Later, the second-order elastic analysis is conducted to get the initial element forces. The reduction factor **τ** for Young's modulus E is determined by the MTM method, following which the updated element stiffness and element forces can be obtained. The element end forces will be checked at each step. If the force point is not located inside the yield surface, it indicates that a plastic hinge is formed in the element ends, and the element plastic reduction matrix will be included in the element stiffness matrix. In this research, a nonlinear solution named Predictor-Corrector is adopted to trace the load-displacement path. This solution has been widely employed by serval researchers, such as Ziemian et al. [34] and Yang et al. [35], and it is a reliable numerical method.

8. Validation

Two groups of verification examples are provided to validate the accuracy of the yield surface generation method and the proposed CP-MTM analysis method. In the first example, two sets of cross-sections, doubly symmetric sections and non-symmetric sections, are studied. The yield surfaces generated by the proposed rigorous cross-section analysis method are validated via the analytical solutions and the well-developed computational method. Then the geometric and material nonlinear analyses for steel members with I-section, Channel section, and non-symmetric cross-section under different boundary and loading conditions are conducted.

8.1 Example 1 – Yield surfaces

8.1.1 Symmetric sections

This example verifies the accuracy of the yield surface generation for symmetrical cross-sections, including a wide flange I-section, a double web section, and a circular hollow section. The dimensions of the cross-sections are given in **Fig. 14**. Those cross-sections were studied by Chen and Atsuta [36]. They provided accurate results of the M_y vs M_z curve under different axial force levels. Same My vs M_z curves are calculated and provided in **Fig. 15**. The load values were normalized to obtain a more general cross-sectional load relationship. Since the sections are doubly symmetric and the full M_y vs M_z curve will also be doubly symmetric, only one-quarter of the resulting curves are given.

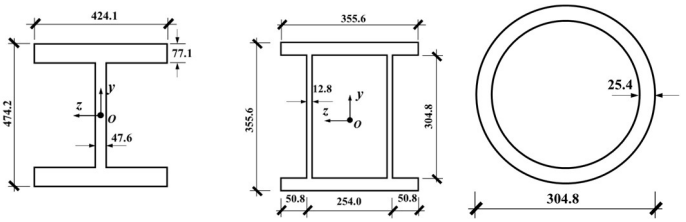

(a) Wide flange I-section (b) Double web section (c) Circular Hollow section

Fig. 14. Doubly symmetric sections (Unit: mm)

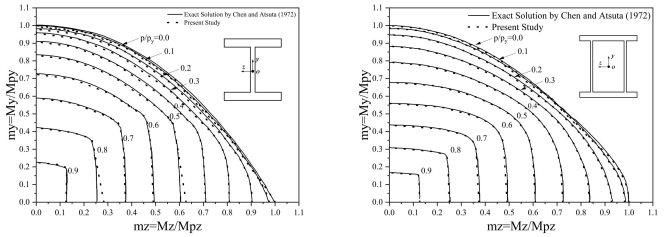

(a) Wide flange section (b) Double web steel section

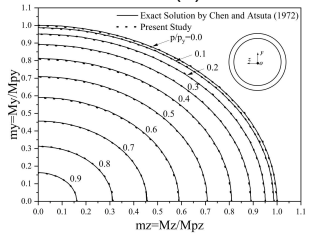

(c) Hollow steel section

Fig. 15. Comparison results for the doubly symmetric sections

The solid lines plotted in **Fig. 15** are the close-formed solutions provided by Chen and Atsuta [36], and the dotted points depict the results from the proposed approach. The results agree with each other well, verifying the validity of the yield surface generation for symmetrical cross-section.

8.1.2Nonsymmetric sections

This example is given to verify the reliability of the proposed yield surface generation method for nonsymmetric sections. Four nonsymmetric sections (**Fig. 16**), including an angle section, a T-section, a nonsymmetric lipped channel section, and a highly irregular section, are studied. The *P-My*, *P-Mz*, *P-Mv*, *P-Mw*, *My–Mz*, and *Mv–Mw* curves generated from the proposed yield surface generation algorithm are compared with those given by the advanced cross-sectional analysis method invented by Liu et al. [20]. Results from the calculation methods recommended by ANSI/AISC-360-16 [31] and McGuire et al. [19] are also plotted in **Fig. 17** to **Fig. 20**.

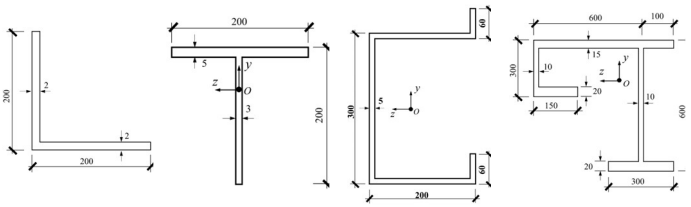

(a) Section A (b) Section B (c) Section C (d) Section D

Fig. 16. Nonsymmetric sections (Unit: mm)

From **Fig. 17**, the results from the proposed algorithm are in line with those from the advanced cross-sectional analysis method given by Liu et al. [20]. While the calculation methods recommended by ANSI/AISC-360-16 [30] and McGuire et al. [19] are no longer suitable for the yield surface generation of nonsymmetric sections. The yield surfaces predicted by the calculation method recommended by ANSI/AISC-360-16 [31] are linear, and most of the yield surfaces are inside the yield surfaces obtained by Liu et al. [20], which means they are safe and conservative. Some figures (**Fig. 19** a, **Fig. 20** a) show that the section capacities predicted by the equation given by McGuire et al. [19] are overestimated. For the equal-leg angel section, the effect of *My* should be equal to the effect of *Mz*, however, the equation given by McGuire et al. generates different results for *My* (**Fig. 19** a) and *Mz* (**Fig. 19** b). This is because the equation given by McGuire et al. (Equation (37)) is proposed for the commonly used symmetric I-section, which is not suitable for the angel section.

$$\varphi = p^2 + {m_z}^2 + {m_y}^4 + 3.5p^2{m_z}^2 + 3p^6{m_y}^2 + 4.5{m_z}^4{m_y}^2 = 1 \quad (37)$$

This example shows the accuracy of the proposed yield surface generation algorithm for nonsymmetric sections and proves that the traditional yield surface calculation methods, such as those equations given by ANSI/AISC-360-16 [31] and McGuire et al. [19], are not suitable for nonsymmetric sections.

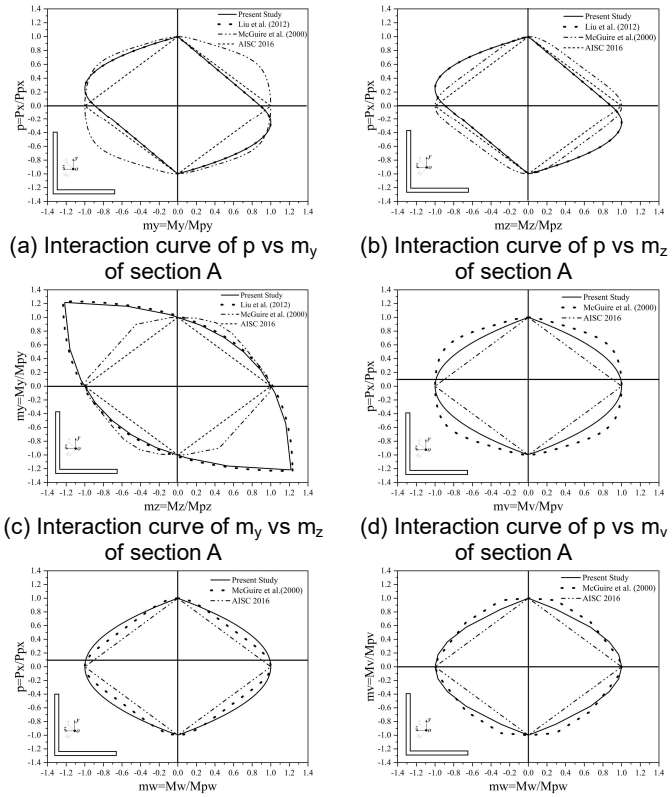

(a) Interaction curve of p vs m_y of section A

(b) Interaction curve of p vs m_z of section A

(c) Interaction curve of m_y vs m_z of section A

(d) Interaction curve of p vs m_v of section A

(e) Interaction curve of p vs m_w of section A

(f) Interaction curve of m_v vs m_w of section A

Fig. 17. Comparison results for section A

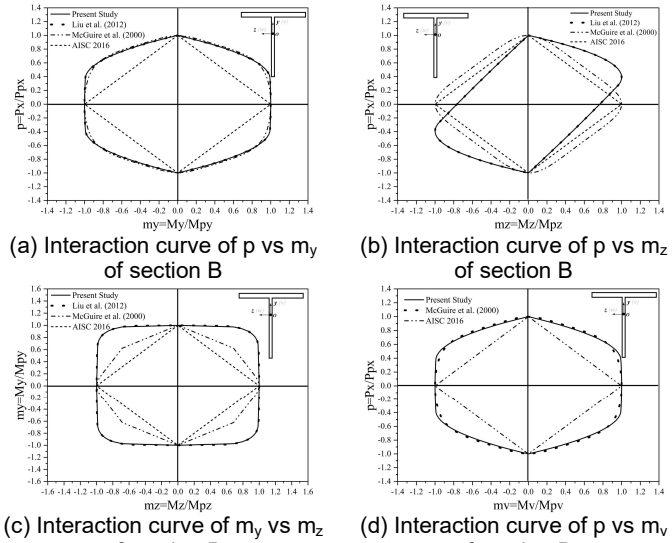

(a) Interaction curve of p vs m_y of section B

(b) Interaction curve of p vs m_z of section B

(c) Interaction curve of m_y vs m_z of section B

(d) Interaction curve of p vs m_v of section B

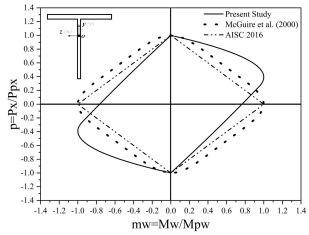

(e) Interaction curve of p vs m_w of section B

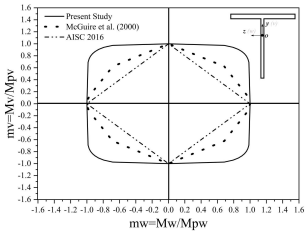

(f) Interaction curve of m_v vs m_w of section B

Fig. 18. Comparison results for section B

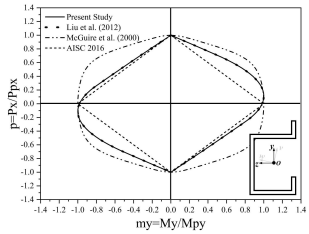

(a) Interaction curve of p vs m_y of section C

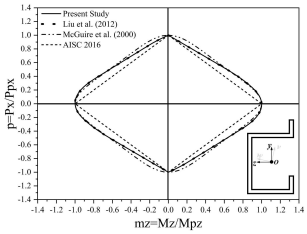

(b) Interaction curve of p vs m_z of section C

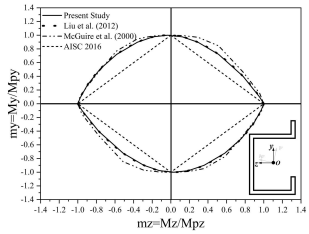

(c) Interaction curve of m_y vs m_z of section C

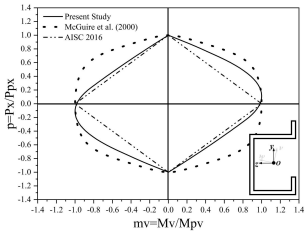

(d) Interaction curve of p vs m_v of section C

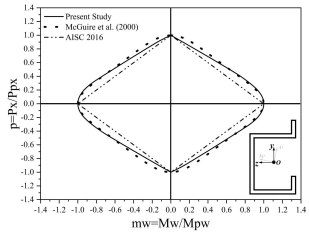

(e) Interaction curve of p vs m_w of section C

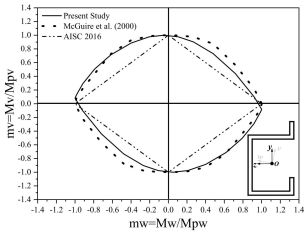

(f) Interaction curve of m_v vs m_w of section C

Fig. 19. Comparison results for section C

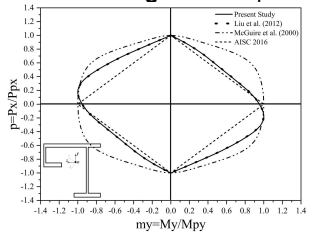

(a) Interaction curve of p_x vs m_y of section D

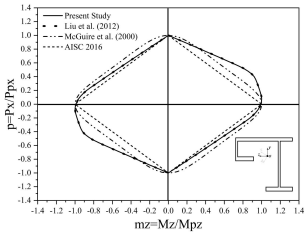

(b) Interaction curve of p_x vs m_z of section D

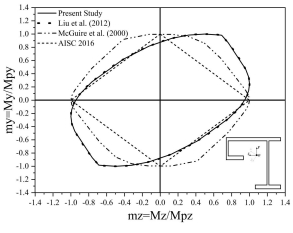

(c) Interaction curve of m_y vs m_z of section D

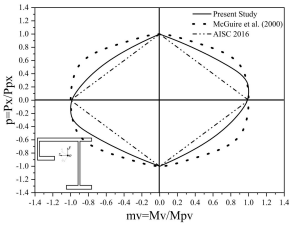

(d) Interaction curve of p_x vs m_v of section D

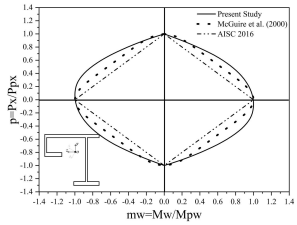

(e) Interaction curve of p_x vs m_w of section D

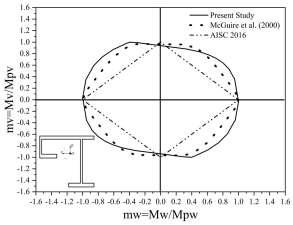

(f) Interaction curve of m_v vs m_w of section D

Fig. 20. Comparison results for section D

8.2 Example 2 –Nonlinear analysis of steel members

The GMNIA for a series of members is conducted to verify the reliability of the proposed CP-MTM analysis method. Members with I-section, Channel section, and nonsymmetric sections under different boundary and loading conditions are investigated. Results from the proposed method and those from other researchers are provided.

8.2.1 I-section beam under bending

A simply supported beam under pure bending has been studied in this example. The beam was initially investigated by Rinchen et al. [13]. The member cross-section and relevant dimensions, the applied forces, and the boundary conditions are given in **Fig. 21**. The boundary conditions at both ends are symmetric. The warping deformations at each end are free, and an additional axial restrain has been employed at the midspan of the beam. The beam has a length of 4.0m, and the material Young's modulus and Poisson's ratio are taken as 200000MPa and 0.3. The material yield stress is 300MPa. The member's initial imperfection has been added by applying a small torque, +970Nmm, about the central axis at the midspan of the beam.

The numerical analysis model Is built in Mastan2 v6 [33] with ten line-elements. There is no residual stress included in this example, and the steel hardening process after firstly reaching yielded is also not considered. The moment-rotation response curves generated by the proposed method and shell elements model proposed by Rinchen et al. [13] are given in **Fig. 21**. The results from Rinchen et al. [13] are taken as benchmarks. Results from the second-order elastic analysis introduced by Liu et al. [14] and those from the conventional approach using the yield surface given by McGuiore et al. are also provided for comparison. From **Fig. 21**, large differences will occur when the second-order elastic analysis is adopted. Meanwhile, a slight increase of end moments will cause significant rotation at the end of the curves, indicating that the beam has formed a plastic hinge. The results generated by inelastic analyses are in line with each other, showing the accuracy of the proposed CP-MTM analysis method.

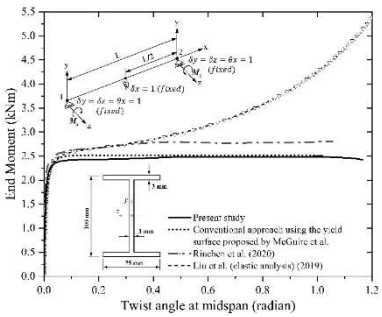

Fig. 21 Post-buckling behavior of the beam.

8.2.2 I-section beam under shear

To further test the accuracy of the proposed method, a fixed-ended beam with I-section is studied. The dimensions of the I-section and the boundary and loading conditions of the beam are given in **Fig. 22**. The beam length is 2743.2 mm, and the Young's modulus and Poisson's ratio of the material are 200,000MPa and 0.3. The material yield strength is 248MPa, and the material hardening stress is ignored. This example was formerly studied by Thai and Kim [7] using the finite element method with fiber beam–column elements, which is a well-established method adopted by researchers [37-39]. This paper created a line-element model in Mastan2 v6 [33], where the beam is modelled with eight elements.

The load-displacement curves generated by the present study, the conventional approach (using the yield surface given by McGuire et al. [19]), and Thai and Kim [7] are plotted in **Fig. 22**. The results given by the sophisticated finite element model built by Thai and Kim [7] are regarded as the benchmark. The comparison of ultimate load factors is listed in **Table 1**. The ultimate load factor calculated by the proposed method has rarely differenced from the benchmark. It is clear from **Fig. 22** that the proposed method can get a reliable result. Only slight differences are observed at the elastoplastic stage, which can be eliminated by adjusting the empirical factors α_v and α_w in the MTM method. Therefore, the proposed method has good accuracy and is applicable for practical applications.

Table 1 Comparison of the predicted ultimate load factor of the beam.

Methods	Ultimate load factor	Difference (%)
Thai and Kim (Shell element) [7]	9.079	-
Thai and Kim (Line-element) [7]	9.003	-0.84
Present	8.932	-1.62

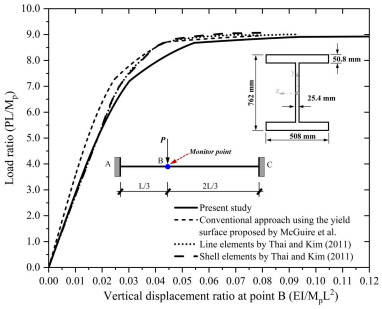

Fig. 22 Load-deflection curve of fixed-ended beam.

8.2.3 Lipped channel section member under bending

In this example, a 4.0m long member with channel cross-section under major axis bending is investigated. The dimensions of the cross-section, and the applied forces and the boundary conditions of the member are given in **Fig. 23**. A torque of +400Nmm is applied at the mid-span of the member as the initial imperfection. The material Young's modulus and Poisson's ratio are 200,000MPa and 0.3. The material yield strength is 500MPa.

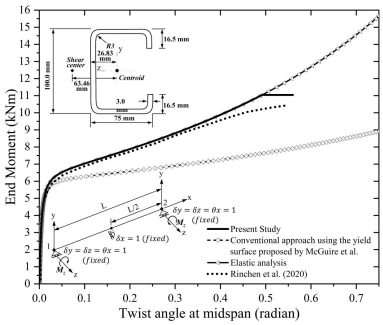

Fig. 23 Post-buckling behavior of the channel member.

This example is firstly studied by Rinchen et al. [13]. The moment-rotation response curves from the shell element model proposed by Rinchen et al. [13] are given in **Fig. 23** as benchmarks. Results from the second-order elastic analysis introduced by Liu et al. [14] and those from the conventional approach (using the yield surface given by McGuire et al. [19]) are also provided for comparison. From **Fig. 23**, the second-order elastic analysis introduced by Liu et al. [14] can predict the elastic and buckling behavior of the member, but large differences will occur when the member enters the elastoplastic stage. Besides, the conventional approach, which is based on the doubly symmetric section assumption, is no longer suitable for the nonlinear analysis of steel members with nonsymmetric sections.

To further validate the reliability of the proposed method, a nonsymmetric lipped channel section member is investigated. The analytical model is the same as the former example, and the cross-section dimensions are shown in **Fig. 24**. The material yield stress is 300MPa, and the initial imperfection is implemented at the mid-span by applying a small twist displacement (+0.007 radians) in this case.

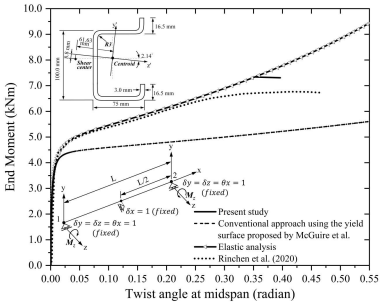

Fig. 24 Post-buckling behavior of the nonsymmetric member.

The moment-rotation response curves from the shell element model proposed by Rinchen et al. [13] are given in **Fig. 24** as benchmarks. The results have further validated that the conventional approach is no longer suitable for the nonlinear analysis of steel members with nonsymmetric sections. They also show that the proposed method can predict the elastoplastic behaviors of nonsymmetric cross-section members accurately.

8.2.4 Angle section column under compression

In this example, four columns with unequal-leg angles, which were investigated by Dinis et al. [40] and Liu et al. [14], have been studied. The material of the columns is steel with ASTM A36 – Grade50, and the Young's modulus and Poisson's ratio are adopted as 205.2Gpa and 0.3. The basic information about the measurement of cross-section dimensions and member lengths can be found in reference literature [40]. As shown in **Fig. 25**, one end of the column is fixed with all degrees of freedoms restrained, and the other end of the column is free in the axial direction with the axial loads applied at the centroid. The initial imperfections and the section properties given by Liu et al. [14] are adopted. Those columns are simulated in Mastan2 v6 [33] with ten line-elements each, to capture the nonlinear behaviors.

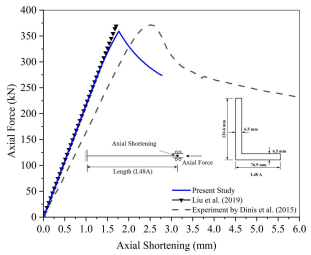

(a) L48A

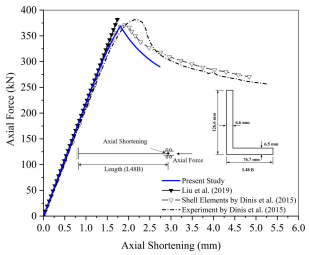

(b) L48B

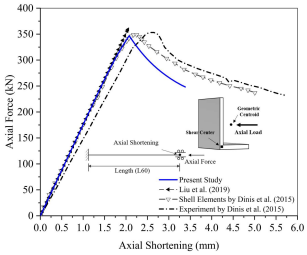

(c) L60

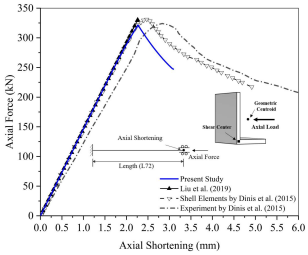

(d) L72

Fig. 25 Load-deflections of the columns

9. Conclusion

The modern structural design methods, namely the direct analysis method in ANSI/AISC-360-16 [31] and GB50017-2017[41], the second-order direct analysis in Hong Kong Steel Code [42], and the others, require the analysis method should be capable of capturing both the geometric and material nonlinear behaviors of the members in a structural system. However, the existing analysis methods are majorly developed for traditional hot-rolled sections with doubly symmetric shapes leading to the direction adoption of these methods for nonsymmetric sections being inappropriate. As a result, in lacking a suitable analysis method, certain obstacles when developing an innovative structural system using nonsymmetric cross-sections limit the potential for higher structural efficiency; for example, the lateral-torsional buckling strengths of beams could be higher when using nonsymmetric section shapes as reported by Sippel et. al [15, 16].

In view of such a need, this research proposed an innovative GMNIA method for designing steel members with symmetric and nonsymmetric sections. This work is expected to contribute to the better and optimal use of innovative cross-section shapes when designing future steel structures. The main features of the present study are summarized as follows.

- An “exact” tangent stiffness matrix is formulated for the nonsymmetric section based on its principal axis and explicitly models the noncoincidence of the shear center and centroid for considering the Wagner effects.
- The CP model is integrated into the element tangent stiffness matrix, and the MTM method has been adopted.
- A rigorous cross-section analysis algorithm is developed for generating the yield surfaces of arbitrary sections.
- An essential matrix is developed to describe the gradients to the yield surface, which further used to control the plastic flow.
- Examples of the implementation of this approach are provided.

Acknowledgement

The work described in this paper was partially supported by grants from the Research Grants Council of the Hong Kong Special Administrative Regain, China (Project No. PolyU/21E/15203121), and a grant from the National Natural Science Foundation of China (No. 52008410).

References

[1]. Driscoll, G.C., Plastic design of multi-story frames. 1965: Fritz Engineering Laboratory.
[2]. Porter, F.L. and G.H. Powell, Static and dynamic analysis of inelastic frame structures. 1971: University of California, College of Engineering, Earthquake Engineering
[3]. King, W., D. White, and W. Chen, Second-order inelastic analysis methods for steel-frame design. Journal of Structural Engineering, 1992. 118(2): p. 408-428.
[4]. Ziemian, R.D., W. McGuire, and G.G. Deierlein, Inelastic limit states design. Part I: Planar frame studies. Journal of Structural Engineering, 1992. 118(9): p. 2532-2549.
[5]. Chen, W. and S.-L. Chan, Second-order inelastic analysis of steel frames using element with midspan and end springs. Journal of Structural Engineering, 1995. 121(3): p. 530-541.
[6]. Liew, J.Y.R., W.F. Chen, and H. Chen, Advanced inelastic analysis of frame structures. Journal of Constructional Steel Research, 2000. 55(1): p. 245-265.
[7]. Thai, H.-T. and S.-E. Kim, Nonlinear inelastic analysis of space frames. Journal of Constructional Steel Research, 2011. 67(4): p. 585-592.
[8]. Liu, S.-W., Y.-P. Liu, and S.-L. Chan, Direct analysis by an arbitrarily-located-plastic-hinge element — Part 1: Planar analysis. Journal of Constructional Steel Research, 2014. 103: p. 303-315.
[9]. Ziemian, R.D. and W. McGuire, Modified tangent modulus approach, a contribution to plastic hinge analysis. Journal of Structural Engineering, 2002. 128(10): p. 1301-1307.
[10]. Mo Hsiao, K. and W. Yi Lin, A co-rotational formulation for thin-walled beams with monosymmetric open section. Computer Methods in Applied Mechanics and Engineering, 2000. 190(8): p. 1163-1185.
[11]. Battini, J.-M. and C. Pacoste, Co-rotational beam elements with warping effects in instability problems. Computer Methods in Applied Mechanics and Engineering, 2002. 191(17): p. 1755-1789.
[12]. Liu, S.-W., R.D. Ziemian, L. Chen, and S.-L. Chan, Bifurcation and large-deflection analyses of thin-walled beam-columns with non-symmetric open-sections. Thin-Walled Structures, 2018. 132: p. 287-301.
[13]. Rinchen, G.J. Hancock, and K.J.R. Rasmussen, Geometric and material nonlinear analysis of thin-walled members with arbitrary open cross-section. Thin-Walled Structures, 2020. 153: p. 106783.
[14]. Liu, S.-W., W.-L. Gao, and R.D. Ziemian, Improved line-element formulations for the stability analysis of arbitrarily-shaped open-section beam-columns. Thin-Walled Structures, 2019. 144: p. 106290.
[15]. Sippel, E.J., R.D. Ziemian, and H.B. Blum, Structural analysis using line elements to model members with non-symmetric cross sections. Thin-Walled Structures, 2021. 169: p. 108407.
[16]. Sippel, E.J. and H.B. Blum, Structural analysis of steel structures with non-symmetric members. Engineering Structures, 2021. 245: p. 112739.
[17]. Du, X. and J. Hajjar, Three-dimensional nonlinear displacement-based beam element for members with asymmetric thin-walled sections. 2020.
[18]. Du, X. and J. Hajjar, Three-dimensional nonlinear displacement-based beam element for members with angle and tee sections. Engineering Structures, 2021. 239: p. 112239.
[19]. McGuire, W., R.H. Gallagher, and R.D. Ziemian, Matrix structural analysis. 2000.
[20]. Liu, S.-W., Y.-P. Liu, and S.-L. Chan, Advanced analysis of hybrid steel and concrete frames: Part 1: Cross-section analysis technique and second-order analysis. Journal of Constructional Steel Research, 2012. 70: p. 326-336.
[21]. Farzanian, S., et al., Geometric imperfection models for CFS structural members, Part I: Comparative review of current models.
[22]. Schafer, B. and T. Peköz, Computational modeling of cold-formed steel: characterizing geometric imperfections and residual stresses. Journal of constructional steel research, 1998. 47(3): p. 193-210.
[23]. Tang, Y.-Q., Y.-P. Liu, and S.-L. Chan, A co-rotational framework for quadrilateral shell elements based on the pure deformational method. Advanced Steel Construction, 2018. 14(1): p. 90-114.
[24]. Schafer, B., Local, distortional, and Euler buckling of thin-walled columns. Journal of structural engineering, 2002. 128(3): p. 289-299.
[25]. Ádány, S. and B. Schafer, Generalized constrained finite strip method for thin-walled members with arbitrary cross-section: Primary modes. Thin-Walled Structures, 2014. 84: p. 150-169.
[26]. Bian, G., K. D. Peterman, S. Torabian, and B. Schafer, Torsion of cold-formed steel lipped channels dominated by warping response. Thin-Walled Structures, 2016. 98: p. 565-577.
[27]. Gao, W.-L., AHA Abdelrahman, S.-W. Liu and R.D. Ziemian, Second-order dynamic time-history analysis of beam-columns with nonsymmetrical thin-walled steel sections. Thin-Walled Structures, 2021. 160: p. 107367.
[28]. Abdelrahman, AHA, Y.-P. Liu, S.-W. Liu, and S.-L Chan, Simulation of thin-walled members with arbitrary-shaped cross-sections for static and dynamic analyses. International Journal of Structural Stability and Dynamics, 2020. 20(12): p. 2050128.

[29]. Chen, L., AHA Abdelrahman, S.-W. Liu, R.D. Ziemian, and S.-L Chan, Gaussian Beam–Column Element Formulation for Large-Deflection Analysis of Steel Members with Open Sections Subjected to Torsion. Journal of Structural Engineering, 2021. 147(12): p. 04021206.
[30]. Chen, L., Gao, W. L., Liu, S. W., Ziemian, R. D., & Chan, S. L. (2022). Geometric and material nonlinear analysis of steel members with nonsymmetric sections. Journal of Constructional Steel Research, 198, 107537.
[31]. AISC, Specification for Structural Steel Buildings ANSI/AISC 360-16. 2016, American Institute of Steel Construction.: Chicago.
[32]. Chen, L., S.-W. Liu, and S.-L. Chan, Divergence-free algorithms for moment-thrust-curvature analysis of arbitrary sections. Steel and Composite Structures, 2017. 25(5): p. 557-569.
[33]. Ziemian, R.D., W. McGuire, and S.-W. Liu, MASTAN2 v6.0. 2021.
[34]. Ziemian, C.W. and R.D. Ziemian, Efficient geometric nonlinear elastic analysis for design of steel structures: Benchmark studies. Journal of Constructional Steel Research, 2021. 186: p. 106870.
[35]. Yang, Y., A. Chen, Y. Yan, and Z Wang, Using only elastic stiffness in nonlinear and postbuckling analysis of structures. International Journal of Structural Stability and Dynamics, 2019. 19(10): p. 1950112.
[36]. Chen, W.F. and T. Atsuta, Interaction equations for biaxially loaded sections. Journal of the Structural Division, 1972. 98(5): p. 1035-1052.
[37]. Papachristidis, A., M. Fragiadakis, and M. Papadrakakis, A 3D fibre beam-column element with shear modelling for the inelastic analysis of steel structures. Computational Mechanics, 2010. 45(6): p. 553-572.
[38]. Ceresa, P., L. Petrini, and R. Pinho, Flexure-shear fiber beam-column elements for modeling frame structures under seismic loading—state of the art. Journal of Earthquake Engineering, 2007. 11(S1): p. 46-88.
[39]. Suzuki, Y. and D. Lignos. Fiber-based model for earthquake-induced collapse simulation of steel frame buildings. in Proceedings of the 11th US national conference on earthquake engineering. 2018.
[40]. Dinis, P.B., D. Camotim, K. Belivanis, C. Roskos, and T. Helwig. On the Buckling, Post-Buckling and Strength Behavior of Thin-Walled Unequal-Leg Angle Columns. in Proceedings of the Annual Stability Conference Structural Stability Research Council: Structural Stability Research Council Nashville, Tennessee. 2015.
[41]. GB50017-2017. Code for design of steel structures. 2017, Ministry of Housing and Urban-Rural Development of the People's Republic of China, General Administration of Quality Supervision, Inspection and Quarantine of the People's Republic of China.
[42]. CoPHK. Code of practice for the structural use of steel. 2011, Buildings Department, Hong Kong SAR Government.